

# Shortwave-Infrared Line-Scan Confocal Microscope for Deep Tissue Imaging in Intact Organs

Jakob G. P. Lingg, Thomas S. Bischof, Bernardo A. Arús, Emily D. Cosco, Ellen M. Sletten, Christopher J. Rowlands, Oliver T. Bruns, and Andriy Chmyrov\*

The development of fluorophores with photoemission beyond 1000 nm provides the opportunity to develop novel fluorescence microscopes sensitive to those wavelengths. Imaging at wavelengths beyond the visible spectrum enables imaging depths of hundreds of microns in intact tissue, making this attractive for volumetric imaging applications. Here, a novel shortwave-infrared line-scan confocal microscope is presented that is capable of deep imaging of biological specimens, as demonstrated by visualization of labeled glomeruli in a fixed uncleared kidney at depths beyond 400 µm. Imaging of brain vasculature labeled with the near-infrared organic dye indocyanine green, the shortwave-infrared organic dye Chrom7, and rare earth-doped nanoparticles is also shown, thus encompassing the entire spectrum detectable by a typical shortwave-infrared sensitive InGaAs detector.

to reject background fluorescence originating from outside of the focal plane. As a result, the image contrast is reduced, and the detection sensitivity is compromised. While many microscopy techniques<sup>[1–6]</sup> can achieve optical sectioning, they are often restricted by either imaging depth, spatial- or temporal resolution, or the geometry of the sample.

One possibility to improve imaging depths in dense tissue is to shift the detection window to longer wavelengths of the electromagnetic spectrum, such as the shortwave-infrared (SWIR, 1000 nm to 2500 nm) wavelength regime. The SWIR provides several advantages in terms of light-tissue interactions for optical imaging such as reduced scattering,

decreased attenuation by blood and pigments, and lower autofluorescence by tissue.<sup>[7]</sup> Those properties make it an attractive detection window for optical microscopy. However, fluorescence imaging in the SWIR still possesses several inherent limitations that impact the amount of collected signal, consequently reducing the temporal resolution of the imaging system compared to

## 1. Introduction

One of the current challenges in optical microscopy is the volumetric imaging of intact organs at significant depths and high spatiotemporal resolution. Ordinary widefield epifluorescence microscopy, while fast, does not address this challenge as it has inadequate optical sectioning – the ability of an imaging system

J. G. P. Lingg  
School of Computation  
Information and Technology  
Technical University of Munich  
85748 Garching, Germany

J. G. P. Lingg, T. S. Bischof, B. A. Arús, O. T. Bruns, A. Chmyrov  
Department of Functional Imaging in Surgical Oncology  
National Center for Tumor Diseases (NCT/UCC)  
01307 Dresden, Germany  
E-mail: andriy.chmyrov@nct-dresden.de

J. G. P. Lingg, T. S. Bischof, B. A. Arús, O. T. Bruns, A. Chmyrov  
German Cancer Research Center (DKFZ)  
69120 Heidelberg, Germany

J. G. P. Lingg, T. S. Bischof, B. A. Arús, O. T. Bruns, A. Chmyrov  
Medizinische Fakultät und University Hospital Carl Gustav Carus  
Technische Universität Dresden  
01307 Dresden, Germany

J. G. P. Lingg, T. S. Bischof, B. A. Arús, O. T. Bruns, A. Chmyrov  
Helmholtz-Zentrum Dresden - Rossendorf (HZDR)  
01328 Dresden, Germany

J. G. P. Lingg, T. S. Bischof, B. A. Arús, E. D. Cosco, O. T. Bruns,  
A. Chmyrov  
Helmholtz Pioneer Campus  
Helmholtz Munich  
85764 Neuherberg, Germany

E. D. Cosco  
Department of Pathology  
Stanford University  
Stanford, CA 94305, USA  
E. D. Cosco, E. M. Sletten  
Department of Chemistry and Biochemistry  
University of California  
Los Angeles, CA 90095, USA

C. J. Rowlands  
Department of Bioengineering  
Imperial College London  
London SW7 2AZ, UK

© 2023 The Authors. Laser & Photonics Reviews published by Wiley-VCH GmbH. This is an open access article under the terms of the Creative Commons Attribution License, which permits use, distribution and reproduction in any medium, provided the original work is properly cited.

DOI: 10.1002/lpor.202300292

visible wavelengths. These limitations arise from multiple factors. Firstly, the labels used for SWIR imaging, such as organic dyes, often have lower quantum yields than their visible counterparts. Secondly, other SWIR labels like quantum dots and rare earth-doped nanoparticles tend to have long lifetimes. When a high photon flux is incident, these labels can quickly reach saturation, and the total fluorescence signal is limited. Moreover, the detectors used for SWIR imaging, typically InGaAs detectors, have higher noise levels than their silicon counterparts used in visible imaging systems. This restricts the sensitivity and thus impacts imaging speed. Nonetheless, the recent developments of SWIR emissive labels<sup>[8–15]</sup> paired with the improvement of SWIR-sensitive detectors<sup>[16,17]</sup> offer the opportunity to develop novel fluorescence microscopes providing optical sectioning with an improved temporal resolution that is sensitive to wavelengths beyond 1000 nm.

SWIR camera-based systems, such as widefield microscopy, have demonstrated *in vivo* imaging depths of up to 800 μm in the brain through cranial windows.<sup>[18]</sup> Further, more advanced widefield techniques requiring image reconstructions have shown millimeter depths through skin and skull.<sup>[19]</sup> Widefield systems provide high pixel rates of hundreds of gigapixels per second (Gpx s<sup>-1</sup>), however the lack of optical sectioning limits its use to thin or sparsely labeled samples. More advanced methods like light-sheet systems<sup>[20,21]</sup> have shown improved optical sectioning by reducing the out-of-focus excitation, nevertheless, the off-axis excitation relative to the detection leads to limitations on the possible geometries of samples, making it ineffective for many *in vivo* applications. In laser-scanning systems, namely confocal and multiphoton,<sup>[22]</sup> the out-of-focus background is suppressed by either the physical rejection of the out-of-focus background by pinholes (confocal) or the non-linear signal generation of multiphoton microscopy. Three-photon microscopy has shown imaging depths in the brain beyond 500 μm through the skull<sup>[23,24]</sup> and depths beyond 1 mm through cranial windows.<sup>[25]</sup> However, as a beam is scanned across the sample in two dimensions, the temporal resolution, especially for larger field-of-views, is reduced relative to widefield systems. Moreover, the high photon flux required for three-photon absorption to occur implies lower repetition rates of the laser, typically between 1 MHz and 4 MHz, compared to the 80 MHz repetition rates used in two-photon microscopy. Thus, three-photon microscopy is typically an order of magnitude slower than two-photon microscopy.

SWIR confocal point-scanning systems<sup>[16,17,26–29]</sup> have demonstrated imaging depths of 600 μm to 1.1 mm for various tissues in fluorescence mode and imaging depths of 1.3 mm through cranial windows in the brain in reflectance.<sup>[29]</sup> However, the reported pixel rates of the fluorescence confocal systems have been between 20<sup>[26]</sup> and 260 kpx s<sup>-1</sup>.<sup>[17]</sup> These rates are relatively low compared to the pixel rates achieved by widefield systems. As a result, when scanning, there is a trade-off between spatial and temporal resolution that must be considered. Although confocal systems might not achieve the imaging speed seen in camera-based systems, their ability to image within the dense sample sets confocal microscopy apart from widefield systems limited either to surface imaging or to very sparsely labeled samples.

One possibility to increase temporal resolution while maintaining optical sectioning is line-scan confocal microscopy. As the name implies, in line-scan confocal, a tightly-focused line is

scanned across the sample instead of a point; the out-of-focus background is suppressed by a slit or rolling shutter instead of a pinhole.<sup>[30–32]</sup> Line-scan confocal microscopes reduce the scan time per frame as there is no need to scan the line along its axis, which dramatically improves imaging speed at the cost of a slight degradation in the 3D point-spread function. Improving the temporal resolution when imaging deep in tissue will allow for rapid z-scanning to acquire volumes. Further, the increased temporal resolution will aid in locating and focusing on the targeted regions of interest. Deep imaging at the cellular level within a living biological system, achievable in the SWIR spectral range, is desired for studying cell-cell interactions in their physiological environment.

On one side, there are multiple currently demonstrated applications of SWIR imaging that do not exhibit fast acquisition speeds, and which would benefit from parallelization of the acquisition (line detection in confocal geometry), such as blood hemodynamics visualization,<sup>[33–35]</sup> cerebrovascular imaging,<sup>[7,9]</sup> and tumor targeting.<sup>[26,36,37]</sup> In addition, fields outside of biology, such as material science,<sup>[38,39]</sup> can benefit from the utility of SWIR confocal imaging.

On the other side, there are numerous examples of fast line-scan confocal microscopy in the visible range, which would benefit from improved achievable penetration depth when using SWIR labels. Examples of those applications include imaging on the subcellular level in model organisms such as *C. elegans* at different stages of development - embryos, larvae, and adults,<sup>[40]</sup> calcium imaging of neuronal activity in mouse brains, voltage imaging of cardiomyocytes in cardiac samples,<sup>[41]</sup> and rapid volumetric imaging.<sup>[42]</sup>

Our work tries to merge these two realms. It demonstrates a way of achieving faster imaging speeds with optical sectioning, due to confocal detection, and extended penetration depth, due to SWIR spectral range.

Here we demonstrate a de-scanned shortwave-infrared line-scan confocal microscope (SWIR LSCM) theoretically capable of achieving pixel rates of up to 250Mpx s<sup>-1</sup>. The microscope is equipped with an InGaAs line detector and is therefore sensitive to shortwave-infrared photoemission of fluorophores. We compare the optical sectioning capabilities of the SWIR LSCM microscope by imaging a liver perfused with fluorescent bacteria on a widefield system and our confocal system. Additionally, we demonstrate the imaging depth of the system by imaging fixed organs, such as the brain and kidneys, labeled with various shortwave-infrared fluorescent probes, namely indocyanine green,<sup>[10]</sup> the chromenylum polymethine dye Chrom7<sup>[43]</sup> and rare earth-doped nanoparticles,<sup>[44]</sup> at depths beyond 400 μm.

## 2. Results

### 2.1. SWIR LSCM System and Image Formation

The experimental setup of the SWIR LSCM is shown in **Figure 1a**. The system is described in detail in the “Methods and Materials” section. In brief, a cylindrical lens shapes the near-infrared excitation beam into a line. A single-axis galvanometer scans the beam before forming the illumination line in the back-focal plane of the objective (25X XSLPLN25XGMP NA 1.0, Olympus; with 4:1 glycerol (3783.1, Roth) to water (Millipore) as

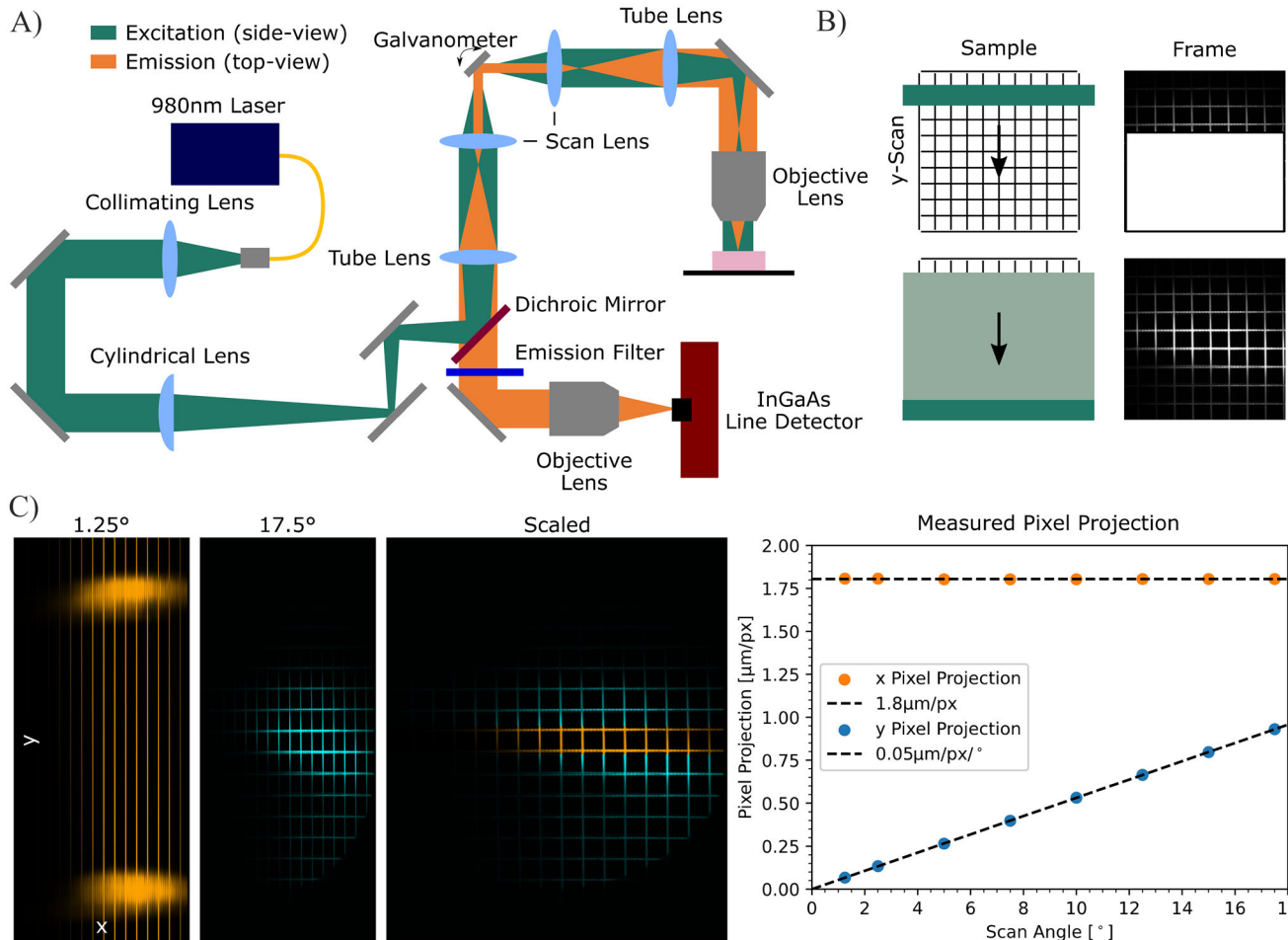


**Figure 1.** SWIR LSCM setup and working principle. A) Schematic of SWIR line-scan confocal microscope. The excitation path is displayed from a side-view perspective, whereas the emission path is depicted from a top-view perspective. B) Explanation of the scan mechanism. A line is scanned from top to bottom (*y*-axis), and the line detector acquires lines and stitches lines to form the final frame. C) 50  $\mu\text{m}$  grid imaged at different scan angles (1.25°, 17.5°), including the overlay of the scaled frames. The plot shows the measured pixel projection per scan angle for the *x*- and *y*-axis.

immersion medium). The epi-collected fluorescence signal is de-scanned by the galvanometer. Finally, an objective lens (4X N4X-PF NA 0.13, Nikon or 2.5X PE IR Plan, Seiya) forms the fluorescence image on the high-speed line camera (Manx 1024 R, Xencis). The use of the line detector removes the need for a slit or a rolling shutter to achieve optical sectioning. We decided to use an optical configuration that does not lead to diffraction-limited imaging and does not make use of the full detector width. The reason is that the larger field of view paired with lower resolution allows for more fluorescence signals to be collected and enables faster imaging on the high-speed InGaAs line detector.

The camera receives two digital signals: the first signal to initialize a frame, followed by signals to trigger the acquisition of single lines. The lines are collected and stitched along the *y*-axis forming a full frame; the scanning mechanism is shown in Figure 1b. Frames are acquired for both the forward and backward scan directions to maximize the frame rate. As the scan range of the galvanometer and the number of lines to be collected per frame can be varied, the resulting images need to be scaled accordingly. Figure 1c displays the frames acquired in re-

flectance of the same grid (50  $\mu\text{m}$  R1L3S3P, Thorlabs) before and after scaling for different scan angles for the same number of lines per frame (1024 lines). The pixel projection per scan angle of the galvanometer in the *x*- and *y*-axis is determined by imaging the grid using a variety of scan angles in reflection. We fit a constant to the pixel projection in the *x*-dimension per scan angle and a linear function to the *y*-dimension pixel projection per scan angle. The *x*-axis pixel projection corresponds to the theoretical pixel projection of 1.8  $\mu\text{m px}^{-1}$  for the corresponding objectives used (25X XSLPLN25XGMP NA 1.0, Olympus; 4X N4X-PF NA 0.13, Nikon), and the pixel size of the line-detector of 12.5  $\mu\text{m}$  ( $12.5\mu\text{m} \times 4 / (25 \times (200 \text{ mm} / 180 \text{ mm})) = 1.8 \mu\text{m}$ ). The *y*-axis pixel projection per scan angle is 0.05  $\mu\text{m px}^{-1}$ . With those coefficients, the acquired images can be scaled for any scan angle.

## 2.2. Resolution and Bacteria Spectra

Due to the lack of commercially available point sources (fluorescent beads, etc.) with photoemission beyond 1000 nm, we

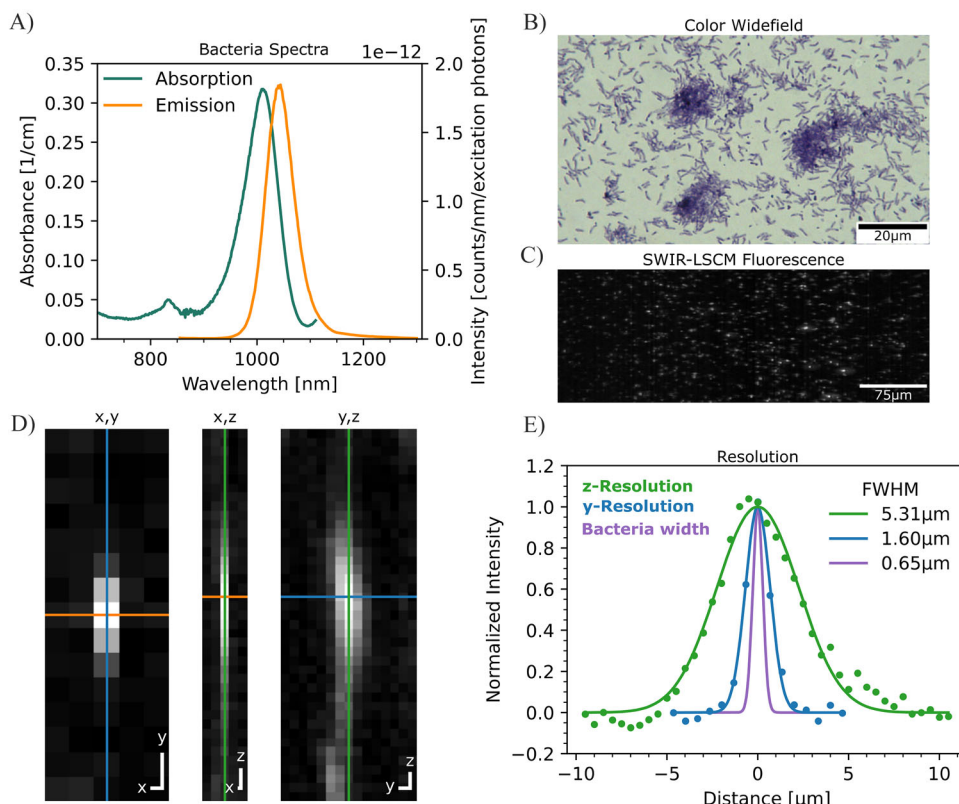


**Figure 2.** Resolution estimation using fluorescent bacteria. A) Absorption and emission properties of the bacteria. B) *B. viridis* stained with crystal violet (IX83 with 100X UPLXAPO100X NA 1.45, Olympus; Imaging Source DFK MKU226-10×22). C) SWIR LSCM acquired maximum intensity projection of 50  $\mu\text{m}$  of bacteria embedded in agarose (excitation wavelength: 980 nm). D) Unscaled image planes of a single bacterium imaged with SWIR LSCM as resolution estimate (1  $\mu\text{m}$  scale bar). E) Resolution estimate plot including the bacterium size as the width of a stained bacterium (purple line), resolution measurement in y-dimension (confocal direction, blue line), and the resolution measurement in z-dimension (green line).

estimated the resolution of the microscope by measuring SWIR fluorescent bacteria (*Blastochloris viridis*, DSM no. 133, DSMZ)<sup>[45]</sup> embedded in agarose. Figure 2a shows the absorption and emission spectra of the bacteria with peaks at 1012 and 1044 nm, respectively. From a widefield image (IX83, 100X UPLXAPO100X NA 1.45, Olympus; Imaging Source DFK MKU226-10 × 22) of the crystal violet-stained bacteria (Figure 2b), we estimate the length of a single bacterium to be between 1.5 and 2.5  $\mu\text{m}$ , the width is estimated to be between 0.5 and 0.8  $\mu\text{m}$ .

We acquired a stack of the bacteria embedded in agarose (a maximum intensity projection of the first 50  $\mu\text{m}$  depth is shown in Figure 2c). A Gaussian curve was fitted through the values of the line profiles passing through the brightest spot of the bacteria sub-stack (Figure 2d). As the bacteria that we used for the PSF measurement are smaller than the resolution measurable due to the sampling frequency (2x pixel projection in  $x = 3.60 \mu\text{m}$ ), it is not possible to accurately estimate the resolution in the  $x$  direction and the value of 3.60  $\mu\text{m}$  serves as the upper bound of it.

The full-width half-maximum of the  $y$ -axis resolution (confocal direction) was measured to be 1.6  $\mu\text{m}$ , and the  $z$ -resolution to be 5.3  $\mu\text{m}$  (Figure 2e).

The sampling step in the  $y$ -direction was 0.67  $\mu\text{m}$ , corresponding to the theoretically measurable resolution of 1.34  $\mu\text{m}$ . However, our objects could not be considered a point source. There-

fore, the measured  $y$ -resolution of 1.6  $\mu\text{m}$  is within the expected range.

The sampling step for  $z$ -scan measurement was 0.25  $\mu\text{m}$ , which would support measurements of resolutions higher than 0.5  $\mu\text{m}$ . Suppose we use the formula for the axial resolution in the point-scanning confocal systems accounting for the pinhole size (1.4 AU in our case).<sup>[46]</sup> In that case, we obtain a theoretical value of 3.0  $\mu\text{m}$ . The discrepancy might come from the non-perfect correction of spherical aberrations in the objectives, as they are designed for imaging applications in the visible spectral range.

### 2.3. Comparison to Widefield Microscopy

We evaluated the optical sectioning capabilities of the SWIR LSCM by imaging the same structure in a fixed mouse liver labeled with fluorescent bacteria on a widefield system and the confocal system (Figure 3). We embedded the liver in agarose in a 35 mm glass bottom dish (81218-200, Ibidi) to simplify the transition and correlation between the inverted widefield system (20× UPLXAPO20x NA 0.8, Olympus) and the confocal system. A narrow tape was adhered to the top of the cover glass to allow positional alignment of the sample in both systems via brightfield imaging on the widefield system and reflectance imaging on

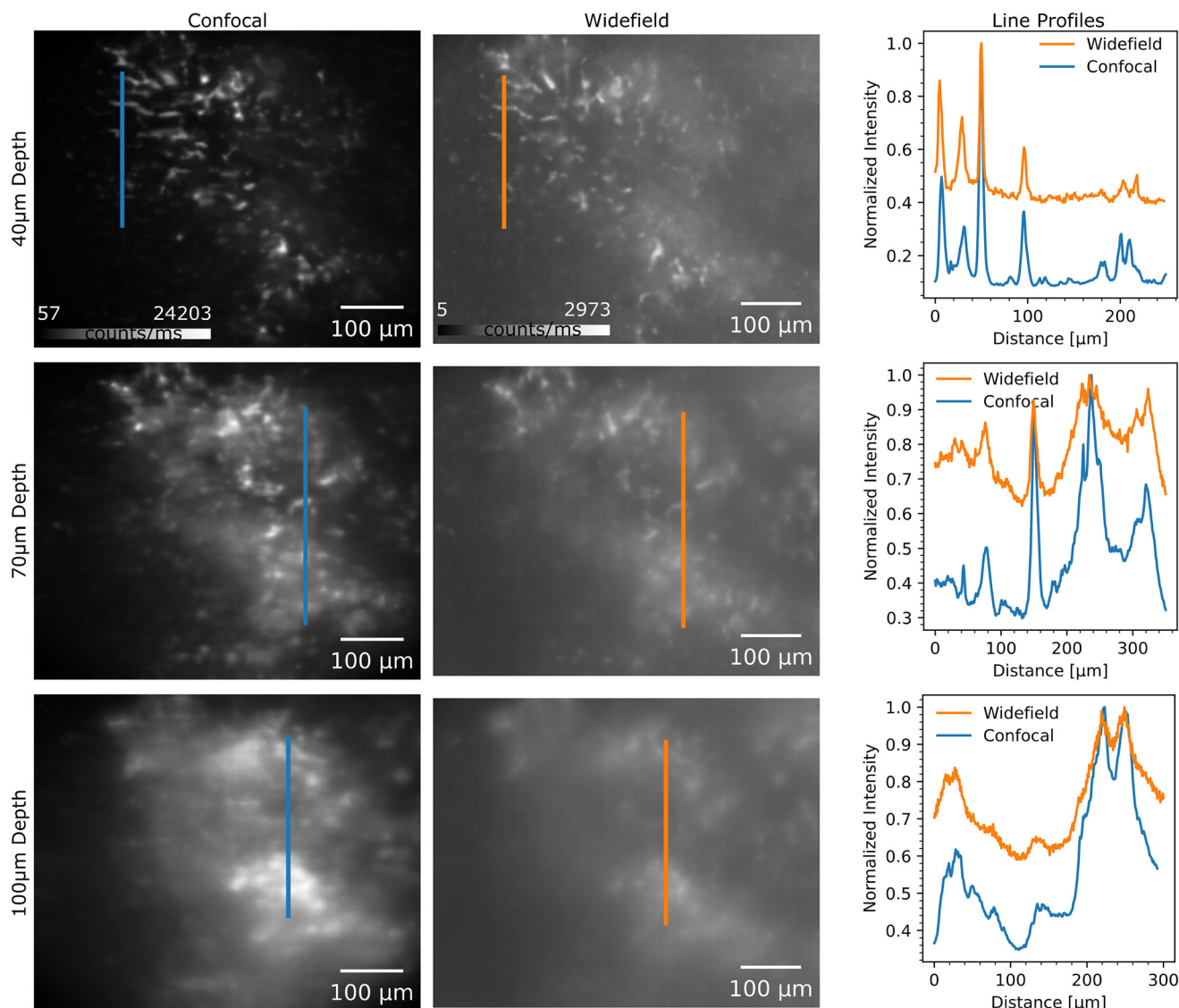


**Figure 3.** Optical sectioning capabilities of SWIR LSCM. Left and center columns: Images of mouse liver perfused with bacteria at different depths taken with both the SWIR LSCM and the widefield system. The colorbar indicates the signal in counts per exposure time; the line exposure time for the SWIR LSCM was 2.2 ms (excitation wavelength: 980 nm, frame height: 1024 lines, galvo frequency: 0.2 Hz, detector width used: 500px, pixel rate: 205 kpx s<sup>-1</sup>, detector gain: 20x) and the widefield exposure time was set to 20 ms on the NIRvana HS, Teledyne. Right column: Intensity-normalized line profiles as shown in the SWIR LSCM and widefield images.

the confocal. Nonetheless, the transition of the sample between the two instruments might have introduced a slight relative tilt of the sample thus leading to marginally different planes being imaged.

We matched the pixel projection of the widefield system ( $\approx 1 \mu\text{m px}^{-1}$ ) by adjusting the scan angle of the confocal system. Both stacks were background and flat-corrected. The SWIR LSCM excitation line has a Gaussian profile. Despite attempts to rectify uneven illumination with a flatfield correction, outcomes may remain imperfect. Replacing the cylindrical lens responsible for forming the excitation line with a Powell lens could effectively minimize uneven excitation.

The acquired frames had a sufficient signal-to-noise ratio. Therefore, no additional rolling ball background subtraction was

applied. From the images alone, here normalized to minimum and maximum values, the contribution of the out-of-focus background is noticeably stronger in the widefield images compared to the confocal images. Vertical line profiles normalized to the maximum were plotted, indicating that the contrast in the confocal images is approximately a factor of three greater than in the images taken with the widefield system. The contrast improvement achieved with a confocal system in the shortwave-infrared aligns with our initial expectations, consistent with previously published work.<sup>[47]</sup> Like the benefits observed when imaging in the visible using confocal techniques over widefield imaging,<sup>[48]</sup> we also see a reduction in the out-of-focus blurring in the shortwave-infrared when imaging in a confocal compared to a widefield configuration.

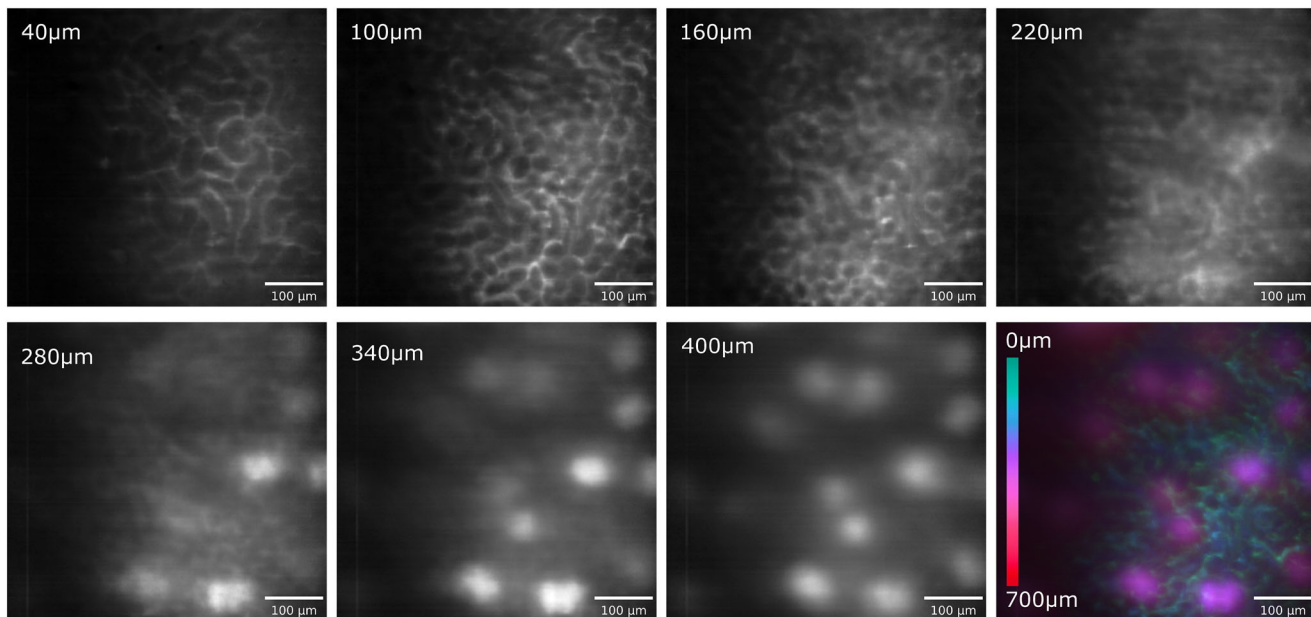


**Figure 4.** Kidney imaging using SWIR LSCM. Sections of intact fixed kidney imaged with SWIR LSCM; the line exposure was set to 11 ms (excitation wavelength: 980 nm, frame height: 512 lines, galvo frequency: 0.08 Hz, detector width used: 730px, pixel rate: 60 kpx s<sup>-1</sup>, detector gain: 20x). Glomeruli are visible in frames past 240 μm depth.

#### 2.4. Kidney Imaging with SWIR LSCM

To further understand the capabilities of the SWIR LSCM, we imaged a fixed mouse kidney whose vasculature was labeled with the shortwave-infrared fluorescent chromenylium polymethine dye Chrom7.<sup>[43]</sup> Chrom7 has an emission peak at  $\approx$ 1000 nm (Figure S1, Supporting Information). The acquired stack, shown in **Figure 4** displays the vasculature of the surface layers of the kidney, and beyond 240 μm of imaging depth, the glomeruli, the structures in which blood is filtered, become visible. We were able to image glomeruli at depths past 400 μm within the fixed kidney; the full stack is displayed in Figure S2 (Supporting Information). The appearance of glomeruli in the images at varying depths again highlights the instrument's optical sectioning capabilities. The diameter size of the glomeruli between 40 μm to 100 μm and the position of the glomeruli at depths beyond 200 μm from the kidney surface corresponds to known literature values.<sup>[49]</sup> We color-coded the stack slices according to the depth<sup>[50]</sup> and performed a maximum intensity projection (MIP) of the colored stacks. This allows us to see the contributions of labeled vessels close to the surface of the kidney and the glomeruli deep within the kidney.

In addition to imaging a kidney stained with Chrom7, we imaged a mouse kidney perfused with the fluorescent bacteria *B. viridis*, which showed an accumulation of the bacteria in the glomeruli (Figure S3, Supporting Information). We verified the labeling of glomeruli with bacteria by imaging cryo-sliced sections of the kidney in fluorescence on the widefield system (using an Olympus 4X UPLAXAPO4X NA 0.16 objective)<sup>[36]</sup> and performing hematoxylin and eosin (H&E) staining of the same section (Figure S4, Supporting Information).

#### 2.5. Brain Imaging with SWIR LSCM

We further demonstrate the capabilities of the SWIR LSCM by imaging mouse brain vasculature labeled via an intravenous injection with 200 μL of 0.05 mg mL<sup>-1</sup> of the clinically approved near-infrared dye indocyanine green (ICG), shown in **Figure 5a**. The injected dose of 0.5 mg k<sup>-1</sup>g matches the clinically recommended dose for humans (0.2 mg k<sup>-1</sup>g – 0.5 mg k<sup>-1</sup>g).<sup>[51]</sup> Upon near-infrared excitation, ICG exhibits strong photoemission well beyond its emission peak ( $\approx$ 830 nm in Methanol, see Figure S1, Supporting Information). Prior work has demonstrated that it is possible to image ICG fluorescence in the spectral range 900 nm to 1600 nm using InGaAs area detectors.<sup>[10]</sup> Here, we employ the InGaAs line detector in our SWIR LSCM, which offers sensitivity from 900 nm to 1650 nm, allowing us to capture images of ICG. The acquired image stack shows a dense vascular structure close to the brain surface, paired with larger vessels. Deeper within the brain, the larger vessels disappear, and capillaries become visible. We were able to reach an imaging depth of 400 μm before losing imaging contrast, as seen in the full stack in Figure S5 (Supporting Information).

As a substitute to ICG, we utilized the shortwave-infrared organic dye Chrom7 to label brain vasculature via intravenous injection of 200 μL of 0.64 mg mL<sup>-1</sup> of Chrom7 formulated into water-soluble poly(ethylene) glycol-phospholipid micelles in saline. Our realized imaging depth was  $\approx$ 400 μm before losing imaging contrast, and we could not distinguish capillaries anymore. The full stack is available in Figure S6 (Supporting Information). To ensure that we reach the maximum imaging depth, we have added a contrast plot and a plot highlighting the signal and background of the acquired z-stack to Figure S7 (Supporting

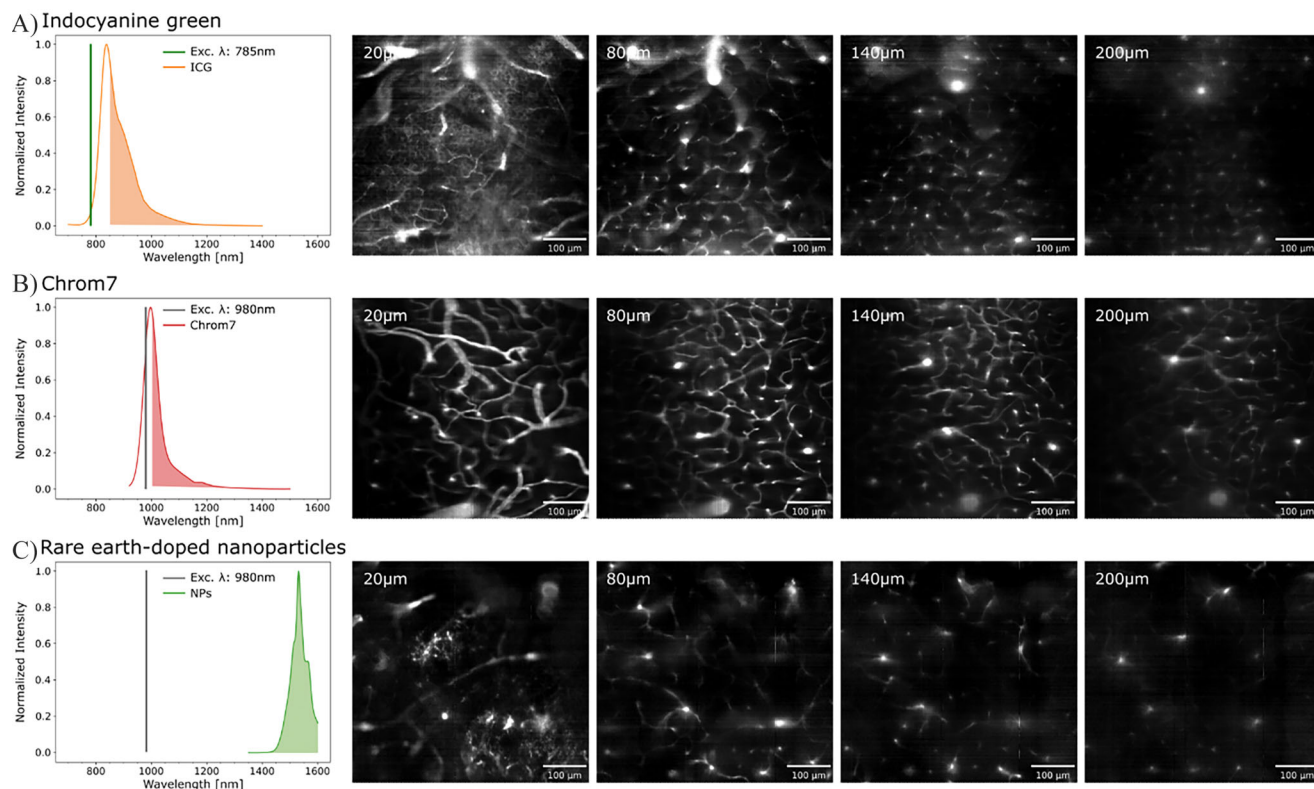


**Figure 5.** Brain vasculature imaging using SWIR LSCM. A) Sections at various depths of fixed mouse brain with ICG-labelled vasculature ( $200 \mu\text{L}$  of  $0.05 \text{ mg mL}^{-1}$  i. v. injection) imaged with  $8.8 \text{ ms}$  line exposure time (excitation wavelength:  $785 \text{ nm}$ , frame height: 512 lines, galvo frequency:  $0.1 \text{ Hz}$ , detector width used:  $730\text{px}$ , pixel rate:  $75 \text{ kpx s}^{-1}$ , detector gain:  $100\times$ , emission filter: FELH0850, Thorlabs). B) Sections of fixed mouse brain labeled with the organic dye Chrom7 in micelles ( $200 \mu\text{L}$  of  $0.64 \text{ mg mL}^{-1}$  i. v. injection) imaged with  $8.8 \text{ ms}$  line exposure time (excitation wavelength:  $980 \text{ nm}$ , frame height: 512 lines, galvo frequency:  $0.1 \text{ Hz}$ , detector width used:  $730\text{px}$ , pixel rate:  $75 \text{ kpx s}^{-1}$ , detector gain:  $100\times$ , emission filter: FELH1000, Thorlabs). C) Sections of rare-earth doped nanoparticle labeled mouse brain micelles ( $200 \mu\text{L}$  of  $20 \text{ mg mL}^{-1}$  i. v. injection) imaged with  $100 \text{ ms}$  line exposure time (excitation wavelength:  $980 \text{ nm}$ , frame height: 512 lines, galvo frequency:  $0.008 \text{ Hz}$ , detector width used:  $730\text{px}$ , pixel rate:  $6 \text{ kpx s}^{-1}$ , detector gain:  $100\times$ , emission filter: FELH1350, Thorlabs).

Information). This analysis reveals that signal is detected over the background at significant depths. However, it is important to note that although we detect signals at great depths, the contrast diminishes. This observation suggests that the achieved imaging depth is primarily attributed to the characteristics of the imaging technique employed rather than the labeling strategy or probe utilized. Further, it appears that the mononuclear phagocytic system takes up Chrom7, which is present in organs that are rich in macrophages, such as the liver. The maximum intensity projection of a stack of liver images displayed in Figure S8b (Supporting Information) reveals cellular labeling with Chrom7.

Finally, we imaged a fixed mouse brain labeled via intravenous injection of  $200 \mu\text{L}$  of  $20 \text{ mg mL}^{-1}$  of rare earth-doped nanoparticles (NBDY-0029A, NIRmidas)<sup>[44]</sup> with an emission peak at  $1550 \text{ nm}$  wavelength (Figure S1, Supporting Information). While the nanoparticles are not prone to bleaching, their inferior brightness, when compared to the acquired ICG or Chrom7 stacks, leads to a loss of detected fluorescence signal, eventually dropping below the noise floor of the InGaAs line-detector when imaging deeper structures. Nonetheless, we were able to image at depths up to  $400 \mu\text{m}$  (Figure S9, Supporting Information).

### 3. Discussion

We developed a microscope that can image hundreds of microns deep into fixed uncleared tissue, which opens many new opportunities in terms of deep tissue imaging in intact dense organs.

We achieved a pixel rate of up to  $1\text{Mpx s}^{-1}$  using our SWIR LSCM for imaging fluorescence in tissue. However, comparable line-scan microscopes operating in the visible, such as the Zeiss LSM 5 LIVE, achieve pixel rates of  $32.5\text{Mpx s}^{-1}$  when imaging fluorescence.<sup>[52]</sup> There are several factors contributing to the performance difference.

The speed of our current system is partly limited by the comparatively high noise floor of the InGaAs detector relative to the noise levels of standard silicon detectors and not yet by the scanning speed of the galvanometer or the line rate of the camera. The dark- and read-noise levels of our utilized InGaAs line detector are higher than those of standard silicon line detectors. Figure S10 (Supporting Information) illustrates the noise levels between a high-end silicon camera (Orca Flash 4.0, Hamamatsu) and the InGaAs line detector we utilized. However, SWIR detectors undergo rapid developments, resulting in notable reductions in noise levels and, consequently, improved detection sensitivity.

Additionally, the low quantum yield of available organic dyes and the long lifetimes of quantum dots and down-conversion rare earth-doped nanoparticles further limit our ability to compete with line-scanning systems operating in the visible wavelength range. While quantum dots have shown promising quantum yields in aqueous media,<sup>[53]</sup> they exhibit much longer photoluminescence lifetimes, typically ranging from 100 ns to 3 μs,<sup>[9,54]</sup> representing orders of magnitude differences from the organic dyes. The lifetimes set limitations on the maximum excitation flux to avoid saturation and affect the overall emission output.

A possibility to overcome the signal limitation is to use labels with increased SWIR brightness, such as aggregation-induced emission (AIE) dots.<sup>[55]</sup> The high brightness of AIE dots was demonstrated to be vital for enabling biomedical applications such as mapping physiological and pathological functions of cortical vasculature and its response to stroke and thrombosis in animals.<sup>[56]</sup> Organic dyes like ICG, while having lower brightness per emitter, have the big advantage of being clinically approved, which significantly reduces the regulatory burden for potential medical applications in humans. Parallelized acquisition allows to trade slower scanning speed for longer acquisition times, thus enabling organic fluorophores use.

To address the limited detected fluorescence from SWIR emissive organic dyes, two strategies could be employed. Firstly, the quantum yield of the dyes could be improved. However, there are fundamental limits imposed by dye physics,<sup>[57]</sup> which may pose a challenge in achieving significant improvements. Alternatively, the emission spectrum of the dyes could be further red-shifted, thereby maximizing the overlap between the quantum efficiency curve of the InGaAs detector and the dye emission spectrum. Figure S11 (Supporting Information) displays the quantum efficiency curve of the employed InGaAs detector, as well as the emission curves of the fluorophores used in this work, highlighting that the overlap between the QE and the emission spectrum of organic dyes, in this case, Chrom7 and ICG, could be further improved.

Nevertheless, we can demonstrate a superior imaging speed of our system compared to a commercially available line-scanning microscope (Zeiss LSM 5 LIVE), specifically when imaging bright artificial samples. We acquired frames of lens paper densely labeled with quantum dots (900737, Sigma-Aldrich) with an emission peak at 1300 nm while moving the stage, capturing images with a resolution of 1024 × 1024 pixels at 120fps. It is worth noting that we only use a pixel width of ≈ 730 pixels from the line detector. Thus, we achieve an effective pixel rate of ≈ 90 Mpx s<sup>-1</sup>. Video S1 (Supporting Information) demonstrates the fast imaging, displayed at a frame rate of 30fps.

Versus multiphoton microscopy, the SWIR LSCM provides more penetration depth compared to two-photon measurements in a fixed kidney of up to 200 μm (see Figure S12, Supporting Information), which are in line with reported two-photon measurements (≈200 μm) in kidneys.<sup>[58]</sup> The linear excitation of the line-scan confocal system leads to larger contributions of out-of-focus excitation, where the laser excitation is sufficient to excite the fluorophores in superficial structures of the tissue, even though it is not focused on this position, reducing the image contrast. Such loss of contrast also forms a limit for achievable imaging depths in multiphoton microscopy.<sup>[59]</sup> In addition, multiphoton processes suffer from loss of efficiency due to pulse

broadening by dispersion, which does not affect single-photon excitation in confocal microscopy. The imaging speed of the multiphoton systems, as with any point-scanning technique, is limited by the scanning speed of the beam scanners and emission rates from the labels. Thus, the field of view must be restricted to be able to image at high temporal resolution. We overcome this issue by parallelizing the acquisition on a line-detector. Generally, our microscope is more cost-effective and easier to implement compared to multiphoton microscopes. Further, line-scan confocal achieves superior optical sectioning capabilities compared to multi-spot confocal and spinning disk confocal systems.<sup>[60]</sup>

SWIR-LCSM is a new technique and there is potential for improvement. Adding more excitation wavelengths to enable the use of multiple fluorophores via excitation multiplexing in the SWIR<sup>[11]</sup> and the addition of a reflectance channel would improve the usability of the instrument. The installation of the reflectance channel would require the addition of polarizing optics to suppress the contribution of internal reflectance arising from the optics,<sup>[29]</sup> potentially leading to transmission losses. To take better advantage of the InGaAs line-detector's width and to be able to increase the pixel projection [μm px<sup>-1</sup>], a different imaging lens, such as one with a 300 mm focal length, could be utilized. This would result in a pixel projection of 0.67 μm px<sup>-1</sup>. However, given our current signal limitations, we have not decreased the pixel projection in our system any further. As the SWIR spectral range is not commonly used in microscopy, additional attention should be paid to the transmission properties of all optical components. Measured transmission curves of various components installed in the SWIR LSCM have been added in Figure S13 (Supporting Information).

In conclusion, SWIR LSCM provides an imaging speed increase of at least a factor of four over point-scanning systems when imaging in tissue. We achieved pixel rates of 205 kpx s<sup>-1</sup> with a detector gain setting of 20× and only used half of the detector width when imaging fluorescent bacteria. Using the same fluorescent label, we can improve the imaging speed further by increasing the detector gain to 100×, leading to pixel rates of 1 Mpx s<sup>-1</sup> while tolerating increased noise levels. Comparable SWIR confocal systems<sup>[16,17,26]</sup> report pixel rates between 20 and 260 kpx s<sup>-1</sup> in fluorescence. Thus, we believe that with the current state of SWIR photoemissive labels and SWIR sensitive detectors, the line-scan imaging configuration is the most viable option to perform optical sectioning in the SWIR with potential dynamic imaging applications in mind.

## 4. Experimental Section

**SWIR LSCM Setup—Bacteria Images:** The excitation beam was emitted by a NIR fiber-coupled laser (BL976-PAG700, Thorlabs controlled by CLD1015, Thorlabs), this laser beam was collimated by a lens (AC254-075-B-ML, Thorlabs). A cylindrical lens (LJ1640L1-B, Thorlabs) shaped the beam into a line. The beam was reflected upwards by a dichroic mirror (DMLP1000, Thorlabs). After passing a tube lens (TTL200-3P, Thorlabs) and scan lens (SL50-3P, Thorlabs) the beam was scanned by a single-axis silver-coated galvanometer (GVS001, Thorlabs). The beam passed a second pair of scan and tube lenses before forming the illumination line in the back-focal plane of the objective (25× XSLPLN25XGMP NA 1.0, Olympus; with 4:1 glycerol (3783.1, Roth) to water (Millipore) as immersion medium). The fluorescence signal was epi-collected by the high NA objective and de-scanned by the galvanometer. The fluorescence signal

passed the dichroic mirror and was spectrally filtered by an emission filter (FELH1000, Thorlabs). An objective lens (4X N4X-PF NA 0.13, Nikon) formed the fluorescence image on the high-speed line camera (Manx 1024 SQ, Xenics) attached to a manual x,z-stage (DT550/M and PT1/M, Thorlabs). To stabilize the temperature of the thermoelectric cooled sensor, a heat sink was attached to the detector, and a cooling fan was positioned (H17543-001, Intel) close to the detector to be able to image consistently at  $-10^{\circ}\text{C}$  detector temperature, resulting in a detector sensitivity range of 900 nm to 1650 nm. A digital acquisition (DAQ) card (PCIe-6351, National Instruments) generated the electrical signals used to drive the galvanometer (triangular wave) and trigger the acquisition of the camera.

The z-scanning by the microscope was performed by moving the objective mounted on a fixed-fixed-single-objective nosepiece (CSN100, Thorlabs) with a motorized focusing module (ZFM2020, Thorlabs). The electronic components (galvanometer, camera, x,y-stage, z-stage) and the acquisition of stacks were controlled by self-written custom software with a graphical user interface (Qt C++). The microscope control code was available at GitLab (<https://gitlab.com/brunslab/swir-line-scan-confocal>). Data exploration was done using ImageJ. Data processing, analysis, and plotting were performed with Python using the code, which is available at <https://gitlab.com/brunslab/manuscript-swir-line-scan-confocal>.

**SWIR LSCM Setup—ICG, Nanoparticle, and Chrom7 Images:** For the ICG, nanoparticle, and Chrom7 data acquisition, the objective lens positioned at the detector was swapped with a 2.5 $\times$  lens (2.5 $\times$  PE IR Plan, Seiya). Further, a different achromat (ACL254-050-B-ML) was used to collimate the beam.

For the nanoparticle image acquisition, an immersion oil ( $n = 1.48$  Type FF, Cargille) was used instead of a glycerol solution, and a 1350 nm long-pass filter (FELH1350, Thorlabs) was placed into the detection path.

Solely for the ICG images, a 785 nm fiber-coupled laser (S4FC785, Thorlabs with P3-780A-FC-2, Thorlabs) was used spectrally cleaned by a short-pass filter (FESH0800, Thorlabs), replaced the two tube lenses (TTL200-2P, Thorlabs), used a different dichroic (DMLP805R, Thorlabs), and used an 850 nm long-pass filter (FELH0850, Thorlabs) in the detection path. Additionally, one of the scan lenses (SL50-2P, Thorlabs) was changed.

The acquired stacks were dark corrected and the frames were divided by the normalized median of a substack of the stack to reduce the detector contributions. Two columns of pixels were removed for the nanoparticle frames shown because the pixels were blinking at the high exposure times applied.

**Pixel Projection Characterization:** The pixel projection per scan angle of the galvanometer was determined by imaging a grid (50  $\mu\text{m}$  R1L3S3P, Thorlabs) using a variety of scan angles in reflection. The images were background corrected to remove the signal attained from internal reflections. For each background corrected image, the sum along the y-axis and the x-axis were taken. The sums were plotted and the peaks in the image, corresponding to grid lines, were found. The distance between the peaks in pixels corresponded to the known distance of the grid lines, in this case, 50  $\mu\text{m}$ . A constant to the pixel projection was fit in the x-dimension per scan angle and a linear function to the y-dimension pixel projection per scan angle.

**Bacteria Resolution Target:** A vial with bacteria in medium (Rhodospirillaceae medium no. 27, DSMZ) was centrifuged, the excess medium removed, and Dulbecco's Phosphate Buffered Saline DPBS (14190-094, Gibco) was added to the bacteria. The bacteria solution was vortexed for several minutes until no bacteria clusters were visible in the solution. The bacteria solution was mixed with 1% agarose solution in a 35 mm glass bottom dish (81218-200, Ibidi). Once the agarose-bacteria mixture solidified, the glass bottom dish was attached to a custom 3D-printed container which then was filled with the immersion medium (4:1 glycerol (3783.1, Roth) to water (Millipore)).

A stack with an axial step size of 0.5  $\mu\text{m}$  was acquired. The stack was dark corrected, before being normalized for bleaching by dividing the frames with the average frame value of the section; this assumes a homogenous and isotropic distribution of bacteria (a maximum intensity projection of the first 50  $\mu\text{m}$  depth was shown in Figure 2b. A rolling ball background correction with a radius of 10px was then applied. A Gaussian

curve was fitted through the values of the line profiles passing through the brightest spot of the bacteria sub-stack.

**Spectra—Absorption Spectrum Bacteria:** The absorption spectrum of the fluorescent bacteria (Figure 2c)) was measured with a UV-VIS-NIR spectrophotometer (Lambda1050+, PerkinElmer) equipped with a 150 mm WB-InGaAs (wideband) integration sphere (L6020364, PerkinElmer). The spectrum of the bacteria in medium was measured in a plastic cuvette (Hach 2629500, 10 mm path length, 1.5 mL); the acquired spectrum was corrected by subtracting the spectrum of the pure medium.

**Spectra—Emission Spectra:** The emission spectra of the samples were measured using a liquid nitrogen-cooled InGaAs line detector (Pylon-IR 1024-1.7, Princeton Instruments) and a Silicon detector (PIXIS: 400BR, Princeton Instruments) attached to a Czerny-Turner spectrograph (HRS-300, Princeton Instruments). ICG, *B. viridis*, and the rare earth-doped nanoparticles were excited with 635 nm, 785 nm, and 980 nm wavelength, respectively (SuperK-Extreme, NKT Photonics filtered with SR-Extended-8HP LLTF Contrast, NKT Photonics). Additionally, the excitation light was spectrally filtered by short-pass filters (ICG: FESH0650, Thorlabs; *B. viridis*: FESH0800, Thorlabs; rare earth-doped nanoparticles: FESH1000, Thorlabs) and focused on the mounted cuvette (Hach 2629500, 10 mm path length, 1.5 mL) by an achromat (AC254-200-AB-ML, Thorlabs). The photoemission was collected using a pair of silver-coated off-axis parabolic mirrors (MPD269-P01 and MPD269-P01-H, Thorlabs) that focus the light onto a multimode fiber (400  $\mu\text{m}$ , 0.39 NA, M28L01, Thorlabs) that entered the spectrograph. Long-pass filters (ICG: FELH0650, Thorlabs; *B. viridis*: FELH0850, Thorlabs; rare earth-doped nanoparticles: FELH1150, Thorlabs) were placed in front of the fiber to suppress the excitation light. Acquired spectra were background corrected and intensity corrected using a calibration lamp (SLS201L/M, Thorlabs), considering the quantum efficiency of the detector and wavelength-dependent transmission losses of the system components. The bacteria spectrum was wavelength binned and normalized for the excitation power (ICG: 0.3 mW; *B. viridis*: 4 mW; rare earth-doped nanoparticles: 3.9 mW) at the sample, resulting in a spectrum in units of counts per wavelength per number of excitation photons. The spectral data of Chrom7 was obtained from the authors of its publication.<sup>[43]</sup>

**Animal Preparation—Bacteria Perfusion:** All animal ethics and protocols were approved by and are in agreement with regulations of the government of Upper Bavaria. A mouse (Athymic Nude (Cr:NU(NCr)-Foxn1<sup>nu</sup>), female, 7 weeks, Charles River) was anesthetized with an i.p. Ketamin Xylazin injection. The blood was flushed out by perfusing the mouse with heparin in PBS (200  $\text{mL}^{-1}$ , 375095–100KU, Merck) through the heart using a continuous flow syringe pump (4  $\text{mL min}^{-1}$ , 4000-X, Chemex). Afterward, 7.5 ml *B. viridis* in PBS (14190-094, Gibco) was flushed through the vasculature using the syringe pump. Organs were extracted and fixed in a Paraformaldehyde solution of 4% in PBS (SC-281692, Santa Cruz Biotechnology).

**Animal Preparation—ICG Injection:** A nude mouse (Cr:NU(NCr)-Foxn1<sup>nu</sup>, female, 6 weeks, Charles River) was injected intravenously with 200  $\mu\text{L}$  of 0.05 mg  $\text{mL}^{-1}$  ICG (7695.3, Roth) in water (L0970-500, Biowest) and immediately sacrificed. The brain was extracted and fixed in a Paraformaldehyde solution of 4% in PBS (SC-281692, Santa Cruz Biotechnology).

**Animal Preparation—Nanoparticle Injection:** A nude mouse (Cr:NU(NCr)-Foxn1<sup>nu</sup>, female, 6 weeks, Charles River) was injected intravenously with 200  $\mu\text{L}$  of 20 mg  $\text{mL}^{-1}$  rare earth-doped nanoparticles (NBDY-0029A, NIRmidas) in PBS and immediately sacrificed. The brain was extracted and fixed in a Paraformaldehyde solution of 4% in PBS (SC-281692, Santa Cruz Biotechnology).

**Animal Preparation—Chrom7 Injection:** A nude mouse (Cr:NU(NCr)-Foxn1<sup>nu</sup>, female, 8 weeks, Charles River) was injected intravenously with 200  $\mu\text{L}$  of 0.64 mg  $\text{mL}^{-1}$  Chrom7 formulated into water-soluble poly(ethylene) glycol-phospholipid micelles in saline,<sup>[43]</sup> and immediately euthanized. The brain, kidney, and liver were extracted and fixed in paraformaldehyde 4% in PBS (SC-281692, Santa Cruz Biotechnology).

**Widefield Imaging:** An inverted widefield microscope (IX83, Olympus) with an InGaAs detector (Nirvana HS, Teledyne or Goldeye-034, Allied Vision) was used to make the comparison between the SWIR LSCM and the

widefield system (Figure 3). The microscope was used to image the cryo-sliced sections of the kidney (Figure S4, Supporting Information) in fluorescence and brightfield configuration (absorption contrast). Excitation light of a NIR laser (980 nm, LU0980D350-U30 AF, Lumics) was coupled via a 30:70 beamsplitter (BS020, Thorlabs) to a light guide into the microscope body. The filter cube used consists of a 1000 nm short-pass filter (FESH1000, Thorlabs), a dichroic mirror (DMLP1000), and a long-pass filter (FELH1050) in the detection path.

## Supporting Information

Supporting Information is available from the Wiley Online Library or from the author.

## Acknowledgements

The author thanks Hannes Rolbieski for the support with animal handling, mouse perfusion, and injection. Further, the authors thank David Kamel for supporting the bacteria culture. The authors acknowledge funding from the Helmholtz Zentrum München, the DFG-Emmy Noether program (no. BR 5355/2-1), the German Federal Ministry of Education and Research (BMBF, project BetterView) and from the CZI Deep Tissue Imaging (DTI-0000000248). J. G. P. Lingg is supported by funding from the Joachim Herz Foundation. E.D. Cosco is supported by the NSF (DGE-1144087) and the Foote Family.

Open access funding enabled and organized by Projekt DEAL.

## Conflict of Interest

The authors declare no conflict of interest.

## Data Availability Statement

The data that support the findings of this study are available from the corresponding author upon reasonable request.

## Keywords

Deep Tissue Imaging, Fluorescence Microscopy, Line-Scanning Confocal Microscopy, Shortwave-Infrared (SWIR) Confocal Microscopy

Received: April 1, 2023

Revised: August 22, 2023

Published online: September 10, 2023

- [1] J.-A. Conchello, J. W. Lichtman, *Nat. Methods* **2005**, *2*, 920.
- [2] F. Helmchen, W. Denk, *Nat. Methods* **2005**, *2*, 932.
- [3] J. Mertz, *Nat. Methods* **2011**, *8*, 811.
- [4] D. Lim, K. K. Chu, J. Mertz, *Opt. Lett.* **2008**, *33*, 1819.
- [5] E. H. K. Stelzer, F. Strobl, B.-J. Chang, F. Preusser, S. Preibisch, K. McDole, R. Fiolka, *Nat. Rev. Meth. Prim.* **2021**, *1*, 73.
- [6] C. Dunsby, *Opt. Express* **2008**, *16*, 20306.
- [7] G. Hong, S. Diao, J. Chang, A. L. Antaris, C. Chen, B. Zhang, S. Zhao, D. N. Atochin, P. L. Huang, K. I. Andreasson, C. J. Kuo, H. Dai, *Nat. Photonics* **2014**, *8*, 723.
- [8] V. G. Bandi, M. P. Luciano, M. Saccoman, N. L. Patel, T. S. Bischof, J. G. P. Lingg, P. T. Tsrunchev, M. N. Nix, B. Ruehle, C. Sanders, L. Riffle, C. M. Robinson, S. Difilippantonio, J. D. Kalen, U. Resch-Genger, J. Ivanic, O. T. Bruns, M. J. Schnermann, *Nat. Methods* **2022**, *19*, 353.

- [9] O. T. Bruns, T. S. Bischof, D. K. Harris, D. Franke, Y. Shi, L. Riedemann, A. Bartelt, F. B. Jaworski, J. A. Carr, C. J. Rowlands, M. W. B. Wilson, O. Chen, H. Wei, G. W. Hwang, D. M. Montana, I. Coropceanu, O. B. Achorn, J. Kloepfer, J. Heeren, P. T. C. So, D. Fukumura, K. F. Jensen, R. K. Jain, M. G. Bawendi, *Nat. Biomed. Eng.* **2017**, *1*, 0056.
- [10] J. A. Carr, D. Franke, J. R. Caram, C. F. Perkinson, M. Saif, V. Askoxyakis, M. Datta, D. Fukumura, R. K. Jain, M. G. Bawendi, O. T. Bruns, *Proc. Natl. Acad. Sci. USA* **2018**, *115*, 4465.
- [11] E. D. Cosco, A. L. Spearman, S. Ramakrishnan, J. G. P. Lingg, M. Saccoman, M. Pengshung, B. A. Arús, K. C. Y. Wong, S. Glasl, V. Ntziachristos, M. Warmer, R. R. McLaughlin, O. T. Bruns, E. M. Sletten, *Nat. Chem.* **2020**, *12*, 1123.
- [12] G. Hong, J. T. Robinson, Y. Zhang, S. Diao, A. L. Antaris, Q. Wang, H. Dai, *Angew. Chem., Int. Ed.* **2012**, *51*, 9818.
- [13] Z. Tao, G. Hong, C. Shinji, C. Chen, S. Diao, A. L. Antaris, B. Zhang, Y. Zou, H. Dai, *Angew. Chem., Int. Ed.* **2013**, *52*, 13002.
- [14] K. Welsher, Z. Liu, S. P. Sherlock, J. T. Robinson, Z. Chen, D. Daranciang, H. Dai, *Nat. Nanotechnol.* **2009**, *4*, 773.
- [15] Q. Yang, Z. Ma, H. Wang, B. Zhou, S. Zhu, Y. Zhong, J. Wang, H. Wan, A. Antaris, R. Ma, X. Zhang, J. Yang, X. Zhang, H. Sun, W. Liu, Y. Liang, H. Dai, *Adv. Mater.* **2017**, *29*, 1605497.
- [16] F. Wang, F. Ren, Z. Ma, L. Qu, R. Gourgues, C. Xu, A. Baghdasaryan, J. Li, I. E. Zadeh, J. W. N. Los, A. Fognini, J. Qin-Dregely, H. Dai, *Nat. Nanotechnol.* **2022**, *17*, 653.
- [17] F. Xia, M. Gevers, A. Fognini, A. T. Mok, B. Li, N. Akbari, I. E. Zadeh, J. Qin-Dregely, C. Xu, *ACS Photonics* **2021**, *8*, 2800.
- [18] Z. Feng, X. Yu, M. Jiang, L. Zhu, Y. Zhang, W. Yang, W. Xi, G. Li, J. Qian, *Theranostics* **2019**, *9*, 5706.
- [19] Q. Zhou, Z. Chen, J. Robin, X.-L. Deán-Ben, D. Razansky, *Optica* **2021**, *8*, 796.
- [20] F. Wang, H. Wan, Z. Ma, Y. Zhong, Q. Sun, Y. Tian, L. Qu, H. Du, M. Zhang, L. Li, H. Ma, J. Luo, Y. Liang, W. J. Li, G. Hong, L. Liu, H. Dai, *Nat. Methods* **2019**, *16*, 545.
- [21] F. Wang, Z. Ma, Y. Zhong, F. Salazar, C. Xu, F. Ren, L. Qu, A. M. Wu, H. Dai, *Proc. Natl. Acad. Sci. USA* **2021**, *118*, 202388118.
- [22] J. Qi, C. Sun, D. Li, H. Zhang, W. Yu, A. Zebibula, J. W. Y. Lam, W. Xi, L. Zhu, F. Cai, P. Wei, C. Zhu, R. T. K. Kwok, L. L. Streich, R. Prevedel, J. Qian, B. Z. Tang, *ACS Nano* **2018**, *12*, 7936.
- [23] T. Wang, D. G. Ouzounov, C. Wu, N. G. Horton, B. Zhang, C.-H. Wu, Y. Zhang, M. J. Schnitzer, C. Xu, *Nat. Methods* **2018**, *15*, 789.
- [24] M. He, D. Li, Z. Zheng, H. Zhang, T. Wu, W. Geng, Z. Hu, Z. Feng, S. Peng, L. Zhu, W. Xi, D. Zhu, B. Z. Tang, J. Qian, *Nano Today* **2022**, *45*, 101536.
- [25] N. G. Horton, K. Wang, D. Kobat, C. G. Clark, F. W. Wise, C. B. Schaffer, C. Xu, *Nat. Photonics* **2013**, *7*, 205.
- [26] H. Wan, J. Yue, S. Zhu, T. Uno, X. Zhang, Q. Yang, K. Yu, G. Hong, J. Wang, L. Li, Z. Ma, H. Gao, Y. Zhong, J. Su, A. L. Antaris, Y. Xia, J. Luo, Y. Liang, H. Dai, *Nat. Commun.* **2018**, *9*, 1171.
- [27] M. Zhang, J. Yue, R. Cui, Z. Ma, H. Wan, F. Wang, S. Zhu, Y. Zhou, Y. Kuang, Y. Zhong, D.-W. Pang, H. Dai, *Proc. Natl. Acad. Sci. USA* **2018**, *115*, 6590.
- [28] S. Zhu, S. Herraiz, J. Yue, M. Zhang, H. Wan, Q. Yang, Z. Ma, Y. Wang, J. He, A. L. Antaris, Y. Zhong, S. Diao, Y. Feng, Y. Zhou, K. Yu, G. Hong, Y. Liang, A. J. Hsueh, H. Dai, *Adv. Mater.* **2018**, *30*, 1705799.
- [29] F. Xia, C. Wu, D. Sinefeld, B. Li, Y. Qin, C. Xu, *Biomed. Opt. Express* **2018**, *9*, 6545.
- [30] K.-B. Im, S. Han, H. Park, D. Kim, B.-M. Kim, *Opt. Express* **2005**, *13*, 5151.
- [31] R. Engelmann, *Nat. Methods* **2006**, *3*, III.
- [32] Q. Zhong, A. Li, R. Jin, D. Zhang, X. Li, X. Jia, Z. Ding, P. Luo, C. Zhou, C. Jiang, Z. Feng, Z. Zhang, H. Gong, J. Yuan, Q. Luo, *Nat. Methods* **2021**, *18*, 309.

- [33] G. Hong, J. C. Lee, J. T. Robinson, U. Raaz, L. Xie, N. F. Huang, J. P. Cooke, H. Dai, *Nat. Med.* **2012**, *18*, 1841.
- [34] A. L. Antaris, H. Chen, S. Diao, Z. Ma, Z. Zhang, S. Zhu, J. Wang, A. X. Lozano, Q. Fan, L. Chew, M. Zhu, K. Cheng, X. Hong, H. Dai, Z. Cheng, *Nat. Commun.* **2017**, *8*, 15269.
- [35] T. Yan, X. Wang, S. Liu, D. Fan, X. Xu, Q. Zeng, H. Xie, X. Yang, S. Zhu, X. Ma, Z. Yuan, X. Chen, *Small Methods* **2022**, *6*, 2201105.
- [36] F. Hu, C. Li, Y. Zhang, M. Wang, D. Wu, Q. Wang, *Nano Res.* **2015**, *8*, 1637.
- [37] A. L. Antaris, H. Chen, K. Cheng, Y. Sun, G. Hong, C. Qu, S. Diao, Z. Deng, X. Hu, B. Zhang, X. Zhang, O. K. Yaghi, Z. R. Alamparambil, X. Hong, Z. Cheng, H. Dai, *Nat. Mater.* **2016**, *15*, 235.
- [38] Y. Sung, W. Wang, *Opt. Lett.* **2023**, *48*, 3993.
- [39] V. Buschmann, E. Errmilov, F. Koberling, M. Loidolt-Krüger, J. Breitlow, H. Kooiman, J. W. N. Los, J. van Willigen, M. Caldarola, A. Fognini, M. U. Castaneda, J. de Wild, B. Vermang, G. Brammertz, R. Erdmann, *Rev. Sci. Instrum.* **2023**, *94*, 033703.
- [40] Y. Wu, X. Han, Y. Su, M. Glidewell, J. S. Daniels, J. Liu, T. Sengupta, I. Rey-Suarez, R. Fischer, A. Patel, C. Combs, J. Sun, X. Wu, R. Christensen, C. Smith, L. Bao, Y. Sun, L. H. Duncan, J. Chen, Y. Pommier, Y.-B. Shi, E. Murphy, S. Roy, A. Upadhyaya, D. Colón-Ramos, P. La Riviere, H. Shroff, *Nature* **2021**, *600*, 279.
- [41] J.-M. Tsang, H. J. Gritton, S. L. Das, T. D. Weber, C. S. Chen, X. Han, J. Mertz, *Biomed. Opt. Express* **2021**, *12*, 1339.
- [42] K. D. Mac, M. M. Qureshi, M. Na, S. Chang, T. J. Eom, H. S. Je, Y. R. Kim, H.-S. Kwon, E. Chung, *Opt. Express* **2022**, *30*, 19152.
- [43] E. D. Cosco, B. A. Arús, A. L. Spearman, T. L. Atallah, I. Lim, O. S. Leland, J. R. Caram, T. S. Bischof, O. T. Bruns, E. M. Sletten, *J. Am. Chem. Soc.* **2021**, *143*, 6836.
- [44] Y. Zhong, Z. Ma, F. Wang, X. Wang, Y. Yang, Y. Liu, X. Zhao, J. Li, H. Du, M. Zhang, Q. Cui, S. Zhu, Q. Sun, H. Wan, Y. Tian, Q. Liu, W. Wang, K. C. Garcia, H. Dai, *Nat. Biotechnol.* **2019**, *37*, 1322.
- [45] Z. Chang, C. Liu, S. Zhao, J. Chen, X. Zhang, H. Tian, Q. Sun, bioRxiv **2022** <https://doi.org/10.1101/2022.03.04.482971>.
- [46] T. WILSON, *J. Microsc.* **2011**, *244*, 113.
- [47] V. Zubkovs, A. Antonucci, N. Schuergers, B. Lambert, A. Latini, R. Ceccarelli, A. Santinelli, A. Rogov, D. Ciepielewski, A. A. Boghossian, *Sci. Rep.* **2018**, *8*, 13770.
- [48] J. Jonkman, C. M. Brown, R. W. Cole, *Methods in Cell Biology* **2014**, *123*, 113.
- [49] B. D. Hann, E. J. Baldelomar, J. R. Charlton, K. M. Bennett, *Amer. J. Physiol.-Renal Physiol.* **2016**, *310*, F1328.
- [50] E. Katrukha, GitHub repository, <https://github.com/UU-cellbiology/ZstackDepthColorCode> (accessed: August 2023)
- [51] J. T. Alander, I. Kaartinen, A. Laakso, T. Pätilä, T. Spillmann, V. V. Tuchirin, M. Venermo, P. Välisuo, *Int. J. Biomed. Imaging* **2012**, *2012*, 940585.
- [52] R. Wolleschensky, B. Zimmermann, M. Kempe, *J. Biomed. Opt.* **2006**, *11*, 064011.
- [53] G. Lee, W. H. Jeong, B. Kim, S. Jeon, A. M. Smith, J. Seo, K. Suzuki, J. Kim, H. Lee, H. Choi, D. S. Chung, J. Choi, H. Choi, S. J. Lim, *Small* **2023**, *202301161*. <https://doi.org/10.1002/smll.202301161>
- [54] C. Cheng, J. Li, X. Cheng, *J. Lumin.* **2017**, *188*, 252.
- [55] J. Qi, C. Sun, A. Zebibula, H. Zhang, R. T. K. Kwok, X. Zhao, W. Xi, J. W. Y. Lam, J. Qian, B. Z. Tang, *Adv. Mater.* **2018**, *30*, 1706856.
- [56] J. Meng, Z. Feng, S. Qian, C. Wang, X. Li, L. Gao, Z. Ding, J. Qian, Z. Liu, *Biomater. Adv.* **2022**, *136*, 212760.
- [57] O. E. Semonin, J. C. Johnson, J. M. Luther, A. G. Midgett, A. J. Nozik, M. C. Beard, *J. Phys. Chem. Lett.* **2010**, *1*, 2445.
- [58] B. A. Molitoris, R. M. Sandoval, *Amer. J. Physiol.-Renal Physiol.* **2005**, *288*, F1084.
- [59] L. Wei, Z. Chen, W. Min, *Biomed. Opt. Express* **2012**, *3*, 1465.
- [60] A. G. York, P. Chandris, D. D. Nogare, J. Head, P. Wawrzusin, R. S. Fischer, A. Chitnis, H. Shroff, *Nat. Methods* **2013**, *10*, 1122.